

The Signature and Elimination of Sediment Reverberations

on Submarine Receiver Functions

Zhang, Ziqi^{1*}, & Olugboji, Tolulope¹

¹UR Seismology Lab, Department of Earth and Environmental Sciences, University of Rochester, NY.



I. Introduction & Motivation

The seismic structure of the normal oceanic lithosphere-asthenosphere system is pivotal to our understanding of global geodynamics and plate tectonics. While the receiver function technique has been successfully applied to high-resolution imaging of sharp discontinuities within and across the lithosphere, it suffers from severe limitations when applied to seafloor seismic recordings. This challenge results from near-surface reverberations obscuring weaker conversions from deeper crust and mantle discontinuities, making structural inference unreliable. The scattered wavefield trapped in the overlying water column and the soft sediment layer generate a loud ringing in receiver function traces, a behaviour that is very pronounced for sediment layers which generate resonance modes at high frequencies, e.g., along the coastal plain or in slow shear-wave sediments. While techniques for removing the water reverberations have long been studied in marine environments (Backus, 1959), and by applying a wavefield decomposition approach, only recently has the water-filter approach been applied to the source-deconvolved receiver function traces aiding interpretation of ocean lithospheric structure. These techniques have focused on removing water-column reverberations, and while the filters are easy to design, no study has yet been applied to removing the sediment reverberations in the deep ocean environments, even though similar techniques have been applied to suppressing sediment reverberations observed on receiver functions obtained from continental seismometers (Yu et al., 2015).

In this study, we design a two-stage filter that suppresses both the water-column and sediment-layer reverberations, the latter being more severe in its effect on receiver function analysis. By using synthetic wavefield modeling, we demonstrate that an appropriate dereverberation filter for removing offending reverberations can be designed by tuning to the relevant elastic properties of the sediment layer. We illustrate our methodology by designing an appropriate dereverberation filter for receiver functions, calculated using ocean bottom seismological (OBS) data, obtained from the *NoMelt* experiment located on mature (~70Ma) Pacific seafloor. We describe how the receiver function results obtained after application of the filter show that the sedimentary layer reverberations can be successfully attenuated and the interpretation of deeper crust or lithospheric layering improved.

II. Identifying Resonance

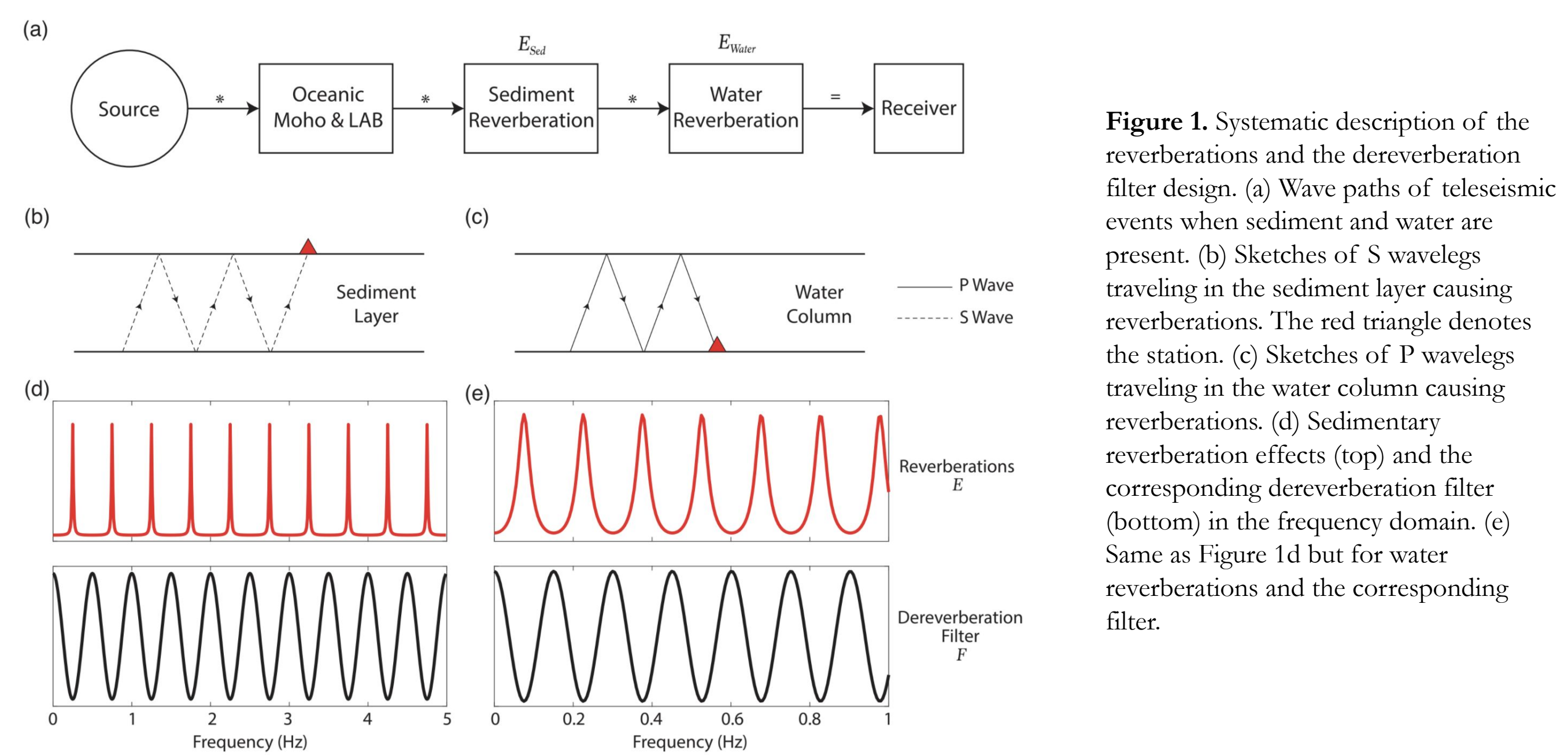


Figure 1. Systematic description of the reverberations and the dereverberation filter design. (a) Wave paths of teleseismic events when sediment and water are present. (b) Sketches of S wavelets traveling in the sediment layer causing reverberations. The red triangle denotes the station. (c) Sketches of P wavelets traveling in the water column causing reverberations. (d) Sedimentary reverberation effects (top) and the corresponding dereverberation filter (bottom) in the frequency domain. (e) Same as Figure 1d but for water reverberations and the corresponding filter.

Receiver function with resonance $R(f) = \tilde{R}(f) \cdot E(f)$
 Receiver function with dereverberation filter applied $\tilde{R}(f) = R(f) \cdot F(f)$
 Dereverberation filter $F(f) = E^{-1}(f) = (1 + r_0 e^{-i2\pi f \Delta t})$

Filter Parameters

r_0 : reflection coefficient at the water-sediment or sediment-crust interface
 Δt : two-way travel time of P wave in water column or S wave in sedimentary layer

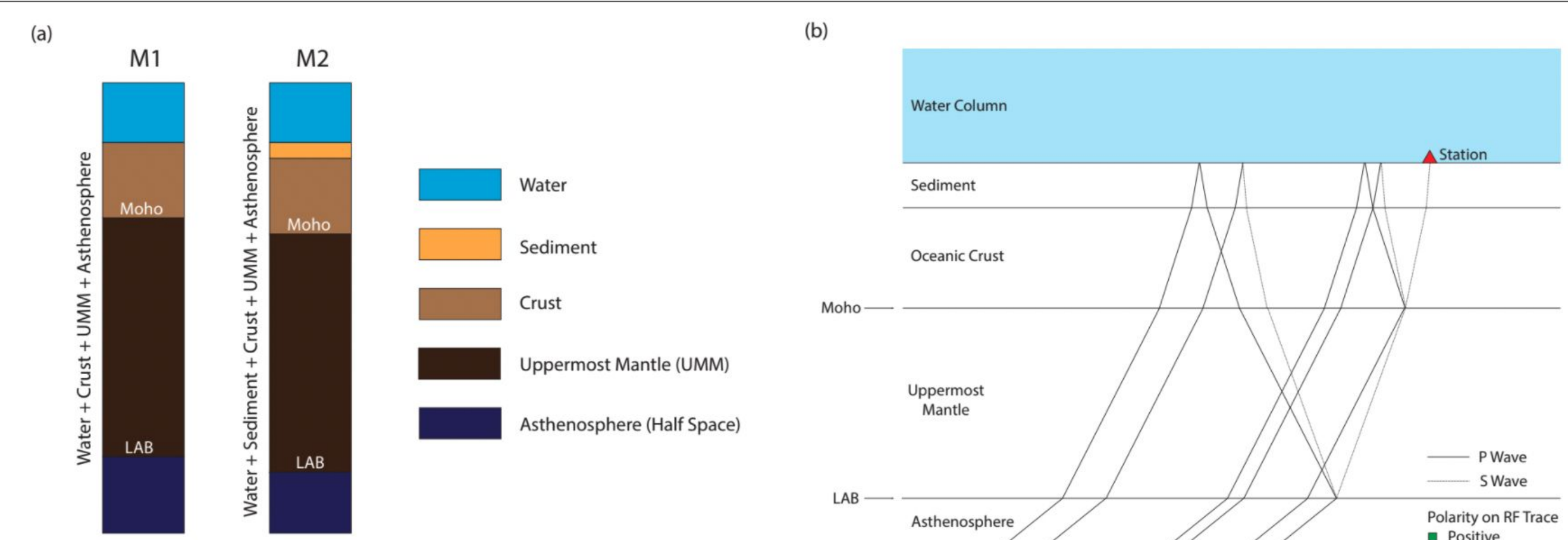


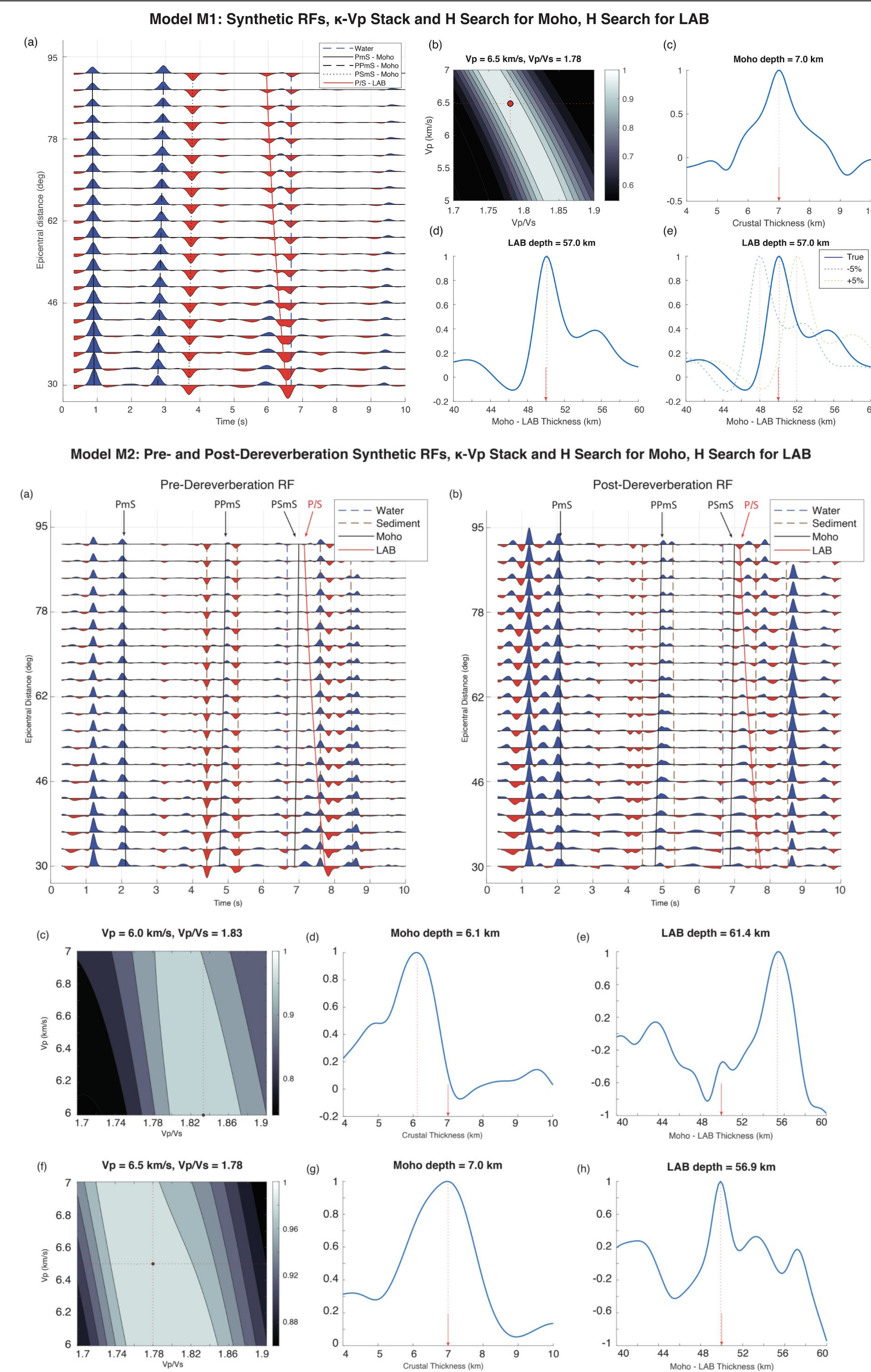
Figure 2. Sketch of velocity models and Ps phases. (a) Representative velocity models used to demonstrate RF estimation in a deep-ocean environment. Model M1 depicts an oceanic crustal and upper mantle structure with no sediments. Model M2 adds a thin sedimentary layer on top of the oceanic crust in both Moho and LAB. Detailed model parameters are shown in Table 1. (b) Schematic diagrams showing the main Ps phases and their multiples from both Moho and LAB, using layered model M2 described in Figure 2a. The names of the phases are labeled next to each ray path; green and brown names indicate positive and negative polarities on the RF traces, respectively.

Table 1. Model parameters of various layers in the synthetic velocity models.

Layer	Density (kg/m ³)	Velocity (km/s)		Velocity Ratio	Thickness (km)	
		v_p	v_s		M1	M2
Water	1027	1.50	-	-	5.0	5.0
Sediment	2000	2.00	0.50	4.00	-	0.8
Crust	2800	6.50	3.65	1.78	7.0	7.0
Uppermost Mantle	3300	8.10	4.50	1.80	50.0	50.0
Asthenosphere	3200	8.10	4.10	1.98	-	-

We compute synthetic receiver functions for two different oceanic plate models, M1 and M2, which highlight the different signatures of a water and sediment layer on receiver function deconvolution. In this implementation, we demonstrate how the dereverberation filter is used to improve the detection of crust and upper mantle interfaces.

III. Synthetic Tests



(Top) Figure 3. Synthetic receiver function traces and parameter search showing recovery of oceanic velocity model M1. (a) RF traces plotted against epicentral distance. RF traces are cut using a time window between 0.2 s and 10 s and re-normalized to emphasize the conversion phases. The predicted arrival times for direct Ps conversions and multiples from the Moho are marked as black solid, dashed and dotted lines, respectively; Ps conversion from the LAB is marked as red solid line; the first water reverberation is marked as blue dashed line. (b) R-vp stack for Moho. (c) Linear search for the depth of Moho. (d) Linear search for the Moho-LAB thickness given the true R and vp from the velocity model (see Table 1). (e) Sensitivity of v_p to uncertainties in mantle velocities. The blue solid line is the same as in Figure 3d; blue and green dashed lines indicate linear search for the Moho-LAB thickness given positive (+5%) and negative (-5%) changes in v_p (relative to the true value defined in Table 1) with fixed true R. The red arrows indicate the true crustal or Moho-LAB thickness of the input model.

(Bottom) Figure 4. Synthetic receiver function traces and parameter search showing recovery of oceanic velocity model M2. (a) Pre-dereverberation RF traces plotted against epicentral distance. RF traces are cut using a time window between 0.2 s and 10 s and re-normalized to emphasize the conversion phases. The predicted arrival times for direct Ps conversions and multiples from the Moho are marked as black solid lines; Ps conversion from the LAB is marked as red solid line; the reverberations from the bottom of sediment are marked as brown dashed lines; the first water reverberation is marked as blue dashed line. (b) Post-dereverberation RF traces plotted against epicentral distance. RF traces are cut using a time window between 0.2 s and 10 s and re-normalized to emphasize the conversion phases. The predicted travel times for different phases are marked the same as Figure 4a. (c) R-vp stack for Moho, using pre-dereverberation RF shown in Figure 4a. (d) Linear search for the depth of Moho, using pre-dereverberation RF shown in Figure 4a. (e) Linear search for the Moho-LAB thickness given the true R and vp from the velocity model (see Table 1), using pre-dereverberation RF shown in Figure 4a. (f) R-vp stack for Moho, using post-dereverberation RF shown in Figure 4b. (g) Linear search for the depth of Moho, using post-dereverberation RF shown in Figure 4b. (h) Linear search for the Moho-LAB thickness given the true R and vp from the velocity model (see Table 1), using post-dereverberation RF shown in Figure 4b. The red arrows indicate the true crustal or Moho-LAB thickness of the input model.

After the synthetic RF traces are filtered using the two-stage dereverberation filters (Figure 4b), the reverberations are suppressed and the identification of the Moho multiple and LAB conversions are improved. The first and strongest Moho multiple, *PPmS*, which was previously masked by the sediment reverberations, is now visible (~4.8 s). The reverberations have been effectively removed, which guarantees that the Moho stack will be reliable. There is also a significant improvement in the seismic LAB conversion (compare *PS* in Figure 4a and 4b), since with sediment reverberations effectively removed, the *PIS* phase can be clearly identified with the correctly predicted positive travel time moveout. We show substantially improved results after applying the appropriate dereverberation filter, using the stack and H search for Moho, and H search for LAB, respectively (compare Figure 4f-h and 4c-e). With clearly identifiable phases, the stacking results are much more reliable and accurate. The resulting crustal P velocity (6.5 km/s), P-to-S velocity ratio (1.78), thickness (7.0 km), and LAB depth (56.9 km) are nearly identical to the input velocity model (compare errors from pre- to post-dereverberation filtering).

IV. Data Example: the *NoMelt* Experiment

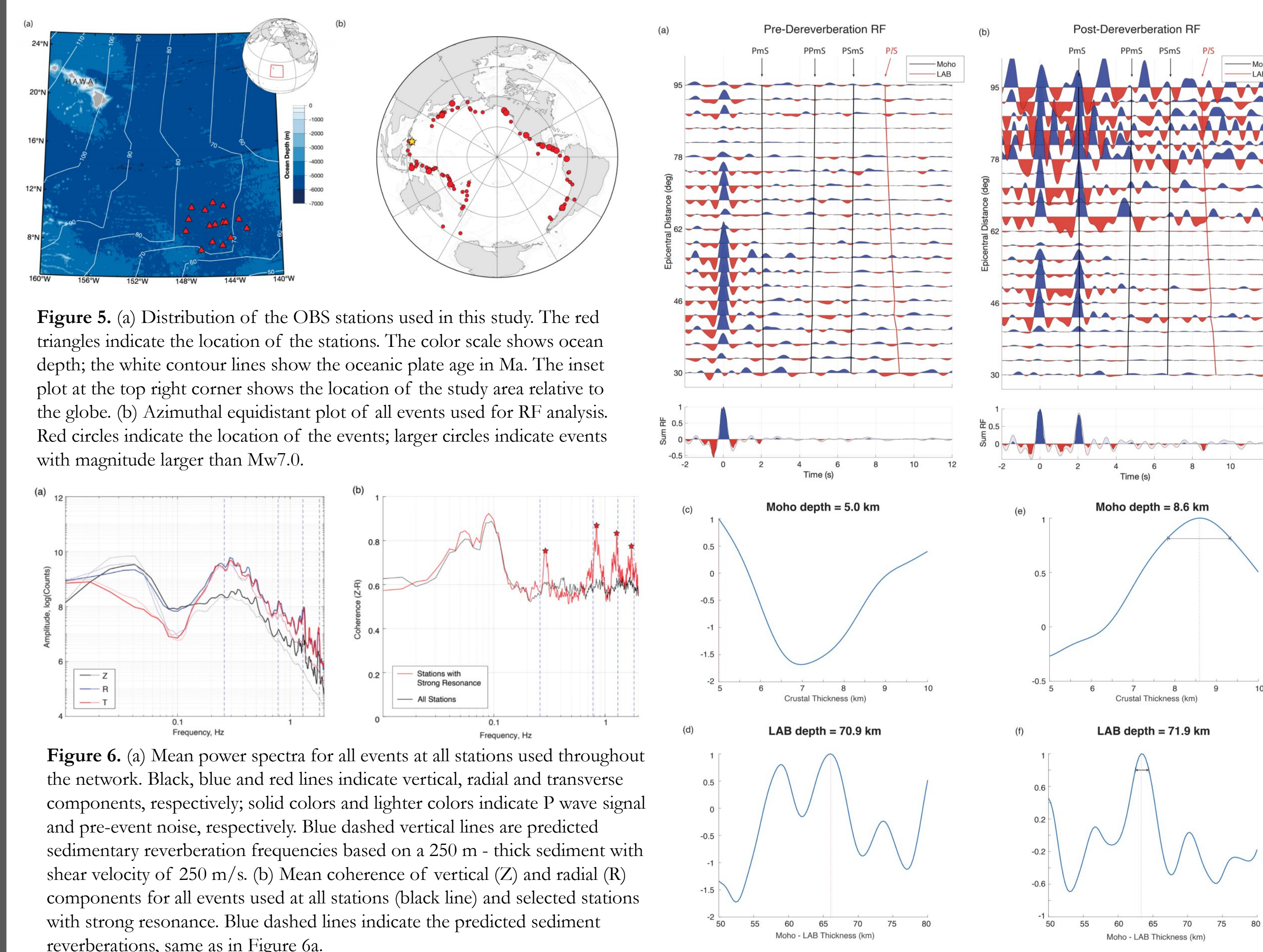


Figure 5. (a) Distribution of the OBS stations used in this study. The red triangles indicate the location of the stations. The color scale shows ocean depth; the white contour lines show the oceanic plate age in Ma. The inset plot at the top right corner shows the location of the study area relative to the globe. (b) Azimuthal equidistant plot of all events used for RF analysis. Red circles indicate the location of the events; larger circles indicate events with magnitude larger than Mw7.0.

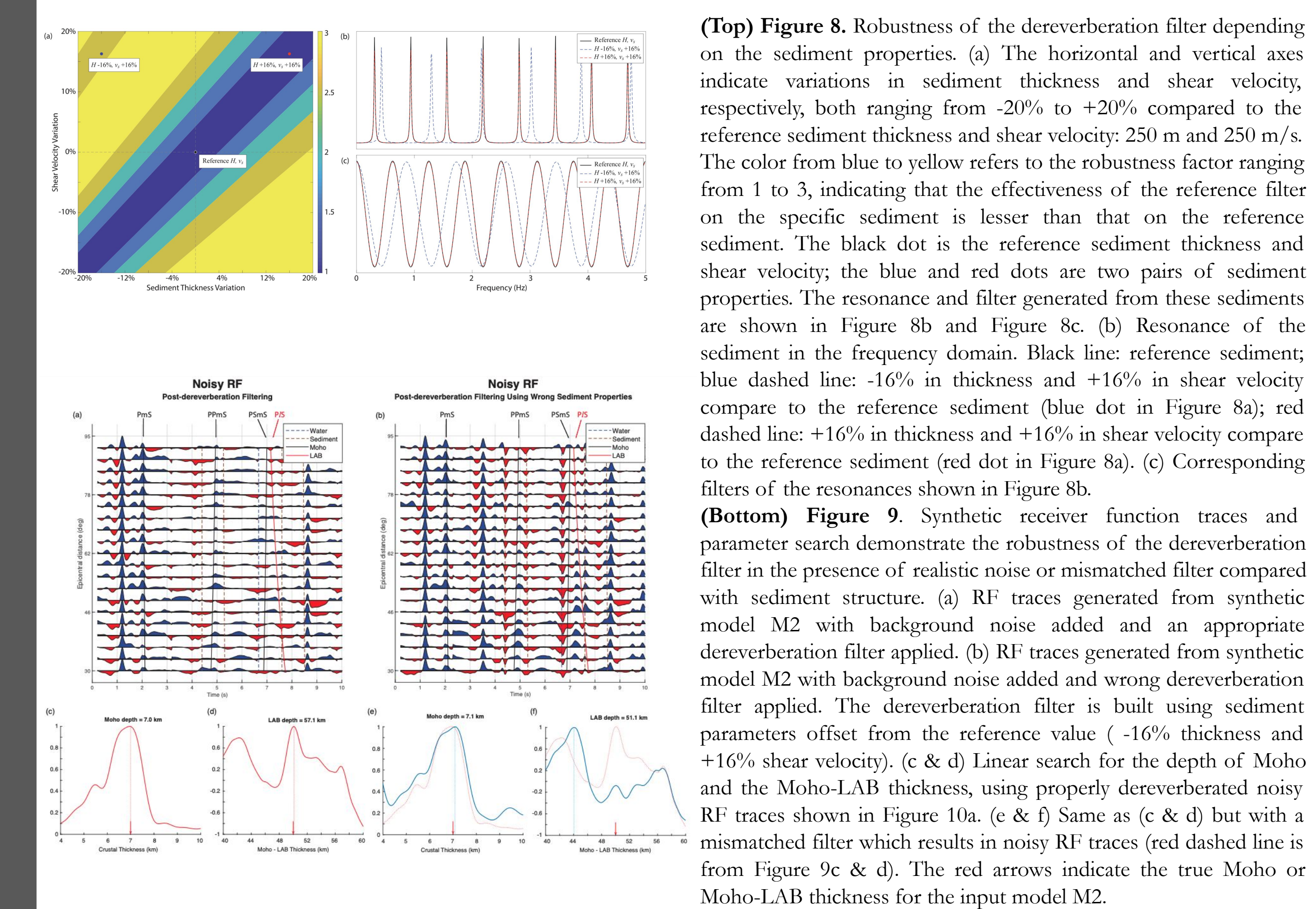
Figure 6. (a) Mean power spectra for all events at all stations used throughout the network. Black, blue and red lines indicate vertical, radial and transverse components, respectively; solid colors and lighter colors indicate P wave signal and pre-event noise, respectively. Blue dashed vertical lines are predicted sedimentary reverberation frequencies based on a 250 m thick sediment with shear velocity of 250 m/s. (b) Mean coherence of vertical (Z) and radial (R) components for all events used at all stations (black line) and selected stations with strong resonance. Blue dashed lines indicate the predicted sediment reverberations, same as in Figure 6a.

Figure 7. Receiver function traces and linear search for Moho and LAB depth using OBS data from *NoMelt*. (a) Pre-dereverberation RF traces plotted against epicentral distance. The predicted arrival times for direct Ps conversions and multiples from the Moho are marked as black solid lines; Ps conversion from the LAB is marked as red solid line. (b) Post-dereverberation RF traces plotted against epicentral distance. The predicted travel times for different phases are marked the same as Figure 7a. Number of events used in each epicentral distance bin is shown in the histogram on the right. (c) Linear search for the depth of Moho given fixed crustal R and vp, using pre-dereverberation RF. (d) Linear search for the Moho-LAB thickness given fixed crustal and mantle R and vp, using pre-dereverberation RF. (e) Linear search for the depth of Moho given fixed crustal R and vp, using post-dereverberation RF. (f) Linear search for the Moho-LAB thickness given fixed crustal and mantle R and vp, using post-dereverberation RF.

Since there are no clear positive peaks at the predicted *PmS* arrival time in the RF traces before applying the dereverberation filter, the H search for Moho using these RFs fails. A search for the seismic LAB gives a depth of 71 km; however, the line-search shows multiple peaks, making it difficult to interpret. The results using RF traces after applying the dereverberation filter gives more reliable results. We recover a crustal thickness of 8.6 ± 0.6 km (Figure 8c). Since the *PIS* phase is clearly visible with correct moveout, the results for the seismic LAB shows an unambiguous major peak at the Moho-LAB thickness of 64 km, giving an LAB depth of 72 ± 1 km.

V. Robustness and Sensitivity

The effectiveness of the dereverberation filter is quantified by a 'robustness' factor that describes how well it matches the reverberation effect of a sediment layer; $\gamma = 1 / \int_0^{0.5H} E(H_s, v_s, f) \cdot | \int_0^{0.5H} F(H_{ref}, v_{ref}, f) |$, where $E(H_s, v_s, f)$ is the reverberation effect in the frequency domain, generated using sediment thickness H_s and shear velocity v_s ; $F(H_{ref}, v_{ref}, f)$ is the filter in the frequency domain generated using the reference sediment properties (250 m & 250 m/s). The mismatch between the filter and reverberations are evaluated to 1.5 Hz, which is the nominal cutoff frequency at which our *NoMelt* receiver functions are calculated.



VI. Discussion & Conclusion

The strength and sharpness of the LAB, in terms of both velocity and depth gradient, can be inferred from the width and amplitude of the pulse associated with the Ps conversion from the LAB (i.e. *PIS* phase) in the receiver functions. *PIS* phase is clearly observed at higher epicentral distance bins after applying the dereverberation filter; the average width of the negative pulse of *PIS* phase is ~0.5 s. For receiver functions calculated at 1.5 Hz, a 0.5 s pulse width implies a relatively sharp transition in depth of no more than 5 km.

The percent velocity drop at the LAB can be predicted from the relative amplitude ratio of the *PmS* and *PIS* phases in the RF traces. The *PIS/PmS* amplitude ratio depends on the velocity contrast across the LAB, following a roughly linear trend. A stronger velocity contrast leads to a larger amplitude for the Ps conversion from the LAB. We place constraints on the *PIS/PmS* amplitude ratio, (0.37 ± 0.13), based on the *PmS* and *PIS* phases clearly visible at ~2s and 9s on the RF traces. We then infer the amplitude ratio from synthetic modeling, suggesting a shear velocity reduction of ~6.8 ± 2.6 % at the LAB in the *NoMelt* region.

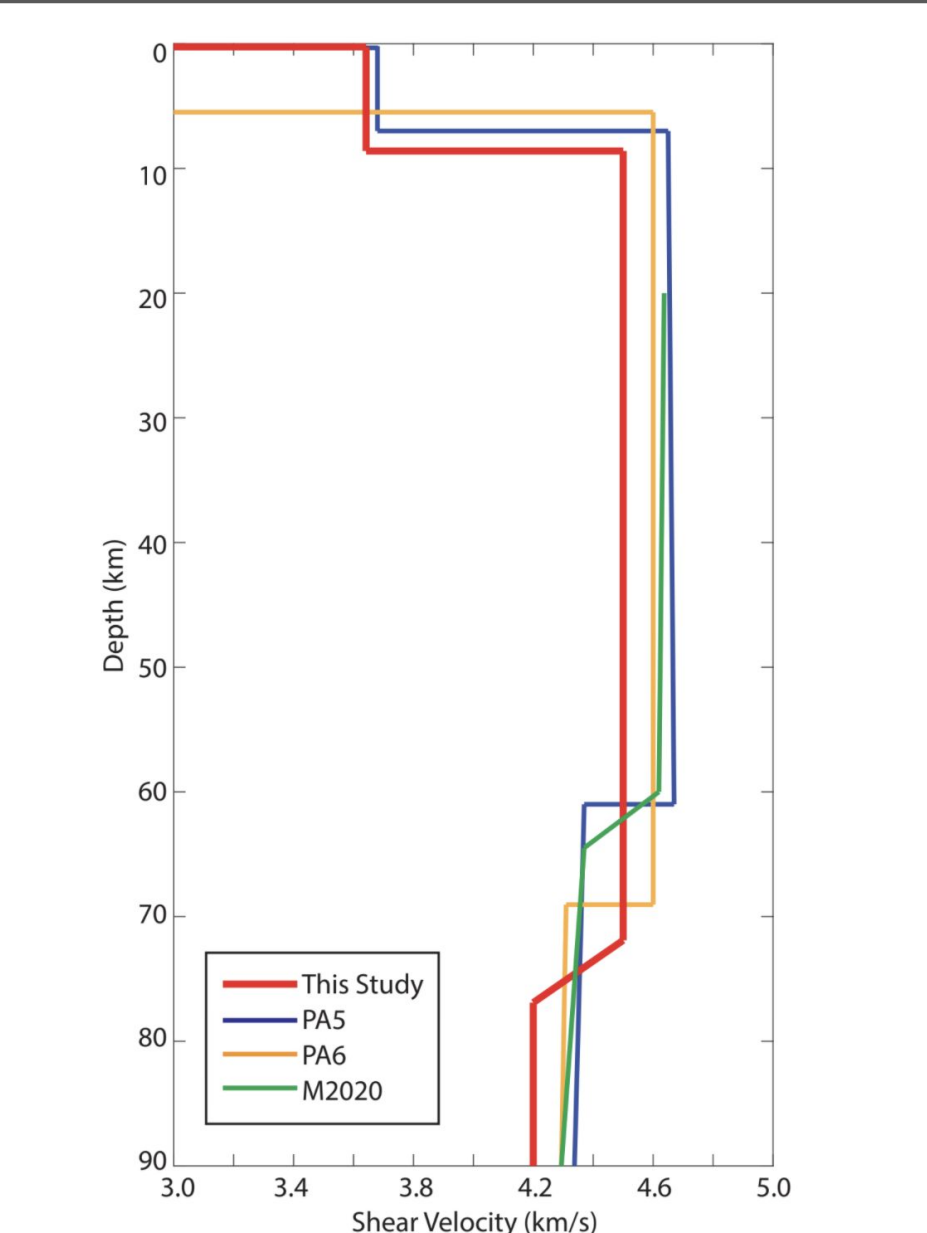


Figure 9. Comparison of shear velocity profiles obtained in this study and some other models: PAS (Gaherty et al., 1996), PA6 (Tan & Helmberger, 2007), and M2020 (Ma et al., 2020).

We show that, with an appropriate dereverberation filter, stable high-resolution receiver function imaging of the lithosphere can be obtained from sea-floor stations and can therefore be used to complement long-wavelength surface wave studies for testing models of oceanic plate origin and evolution. We used multi-taper spectral analysis to improve the detection of earthquake signals buried in noisy data and to validate the parameters of our filter. We confirm that the expected resonance frequencies for the sedimentary layer matches the spectra and coherence pattern of seismic data. The application of a dereverberation filter to the receiver functions will be useful for a growing fleet of ocean bottom deployments and can advance our understanding of the origin and nature of the seismic lithosphere asthenosphere boundary in the oceanic plates. In application to newly collected marine seismic data, we anticipate that post-processing the receiver functions using the recommended dereverberation filter will improve scattered wave imaging, especially with amphibious seismic arrays where the water and sediment layer is expected to vary significantly.

References

Backus, M. M. (1959). Water reverberations—their nature and elimination. *Geophysics*, 24(2), 233–261.
 Gaherty, J. B., Jordan, T. H., & Gee, L. S. (1996). Seismic structure of the upper mantle in a central Pacific corridor. *Journal of Geophysical Research*, 101(B10), 22291.
 Ma, Z., Dalton, C. A., Russell, J. B., Gaherty, J. B., Hirth, G., & Forsyth, D. W. (2020). Shear attenuation and anelastic mechanisms in the central Pacific upper mantle. *Earth and Planetary Science Letters*, 536, 116148.
 Tan, Y., & Helmberger, D. V. (2007). Trans-Pacific upper mantle shear velocity structure. *Journal of Geophysical Research (Solid Earth)*, 112(B8).
 Yu, Y., Song, J., Liu, K. H., & Gao, S. S. (2015). Determining crustal structure beneath seismic stations overlying a low-velocity sedimentary layer using receiver functions. *Journal of Geophysical Research (Solid Earth)*, 120(5), 3208–3218.